

Research Article

Computational Behavior of Trihybrid Casson Nanofluid Blood Flow Occurring Inside the Conical Gap Between the Rotating Disk and the Cone

Yasir Mehmood¹, Waseem Abbasi², Musaed Alhussein³, Khursheed Aurangzeb³, Asia Rehman¹,
Muhammad Shahid Anwar^{4*}

¹Department of Mathematics and Statistics, The University of Lahore, Sargodha, Pakistan

²Department of Computer Science, The University of Lahore, Sargodha, Pakistan

³Department of Computer Engineering, College of Computer and Information Sciences, King Saud University, Riyadh, Kingdom of Saudi Arabia

⁴Department of AI and Software, Gachon University, Seongnam-Si, South Korea
E-mail: shahidanwar786@gachon.ac.kr

Received: 11 July 2024; **Revised:** 18 August 2024; **Accepted:** 28 August 2024

Abstract: The investigation of the flow patterns of a trihybrid nanofluid flow situated in the conical gap that is created among a revolving disc and a stationary cone computationally examined in this study. Three different types of nanoparticles, Al_2O_3 , TiO_2 and Ag are examined with blood as the base fluid according to flow properties and energy phenomenon. While discussing the heat transfer mechanism in trihybrid nanofluid flow crossing through the disc and cone, four different types of cases are explored likewise the disc and cone may be rotating at the same rate or at different rates, or one may be stationary about the other. The numerical scheme is planted to observe the fluid flow and heat transfer patterns. In the current article, we investigated rheological parameters, including rotating speed, cone angle, and concentration of nanoparticles, and the effect of heat transfer performance over velocity and temperature patterns. The results shed light on the complex interactions between the geometric and nanofluid characteristics, providing useful information for fluid dynamics and thermal management applications. This fluid model is also useful for the study of blood pressure, arthritis, brain therapy, and malignant tumors. The graphs are plotted using the MATLAB program BVP4C to ensure convergence. Several variables, such as a magnetic parameter, Prandtl's number, and Reynold's number, have an impact on temperature and velocity profiles. It is evident that the amalgamation of the fraction of three nanoparticles reduces the velocity and enhances the temperature of the nanofluid. The momentum boundary layer expands when the cone and disc rotate in the same direction.

Keywords: trihybrid nanofluid, magnetohydrodynamics, cone, rotating disk, blood flow

MSC: 65L05, 34K06, 34K28

Nomenclature

Symbols

B_o	Magnetic strength
k_{thnf}	Thermal conductivity
z	Axial distance
$F(\eta)$	Axial velocity
$G(\eta)$	Radial velocity
$H(\eta)$	Azimuthal velocity
T	Temperature
Pr	Prandtl number
n	Surface temperature power index
Re	Reynold's number
r	Radial distance
p	Pressure
M	Magnetic parameter
T_w	Surface temperature
T_∞	Free temperature

Greek symbols

ν_{thnf}	Dynamic viscosity of trihybrid nanofluid
ρ_f	Density of fluid
ρ_{thnf}	Density of trihybrid nanofluid
μ_f	Dynamic viscosity of fluid
$(C_p)_{thnf}$	Specific heat of trihybrid nanofluid
$(\sigma)_{thnf}$	Electrical conductivity of trihybrid nanofluid
$\theta(\eta)$	Dimensionless temperature
β	Coefficient of non-Newtonian Casson fluid
$\phi_{Al_2O_3}$	Volumetric fractional parameter
ϕ_{Ag}	Volumetric fractional parameter
ϕ_{TiO_2}	Volumetric fractional parameter
Re_ω	Local Reynold's number
Re_Ω	Local Reynold's number
ω	Angular velocity along disk
Ω	Angular velocity along cone

1. Introduction

The disk-cone apparatus is important in terms of technology and applications, according to the literature. One of the most extensively researched problems in fluid dynamics is the rotating disc problem. A lot of engineering applications are monitored while discussing the flow in the middle of the disc and moving cone as investigated by Spruell and Baker [1]. Also, the fluid viscosity calculations and a creeping flows stability analysis were discussed by Phan-Thien [2]. The construction of industrial machinery such as heat exchangers, geothermal reservoirs, and nuclear waste disposal tanks requires heating and mass transmission along a revolving cone. Researchers studied how rotational speed, fluid viscosity, and cone angle affected the flow field and compared their findings to comparable observations.

A special kind of fluid is called a hybrid nanofluid that is created by deploying a combination of nanoparticles in a base fluid. The base fluid is a well known fluid with chemical and physical properties likewise oil, water, and blood. Comparing hybrid nanofluids to more common fluids like water and oil, trihybrid nanofluids are a special kind of fluid

that performs well in force transfer as compared to hybrid nanofluid flow. Different kinds of thermal activities can utilize the nanofluids when the heat intensity is strong enough as examined by Wahid et al. [3] and Madhukesh et al. [4]. In general, trihybrid nanofluid suggests an encouraging solution for enhancing the presentation of heat transfer system in different applications, this phenomenon potentially has a big impact on sustainability and energy efficiency. It has also been stated that nanofluids can function as smart fluids with targeted or enhanced heat transfer. The water-based fluid in which carbon nanotubes float rises through a vertical cone was studied by Ellahi et al. [5]. With the effect of mass and heat transmission, Turkyilmazoglu [6] investigated the Buongiorno model of nanofluid. Through a thin needle that is flowing in a mixture of nanomaterials and also propelled by viscous dissipation and thermal radiation were discussed by Nazar et al. [7]. Bilal et al. [8] looked into the Williamson nanofluid flow over an expanding sheet in a non-Newtonian manner. The consequences of changing viscosity, thermal and solutal stratification, and Ohmic dissipation were all taken into account due to the enhanced temperature transmission. The heat transmission rate increases from 6.3 to 12.4% when silver nanoparticles of 0.05 volume fraction that was disseminated in water. Using different nanoparticles to extend the heat propagation of the liquid was discussed by Zhao et al. [9]. Sarada et al. [10] examined the suspension of titanium dioxide and graphene oxide nanoparticles that were applied in a porous medium to study the impact of initiation energy on Casson fluid for Darcy-Forchheimer flow, by utilising a base fluid of 50% ethylene glycol. Khan et al. [11] investigated a hybrid nanofluid for the Marangoni convection that comprises a base fluid for two nanoparticles.

The surface boundary flow upon a revolving disk is a conventional problem in fluid mechanics. When a fluid is in contact with a rotating disk, the fluid around the outer layer of the disk seeks observation of a tangential stress caused by the motion of the disk. The present tangential stress originates a boundary layer, which is in the area of fluid near the surface of the disk where the speed of the fluid modifies from zero at the surface to the ambient flow velocity away at a space from the surface. The boundary layer flow across a spinning disk can be interpreted by using the Navier-Stokes equations, which are the fundamental equations of fluid dynamics. On the contrary, due to the complexity of the problem, analytical solutions to these equations are not every time attainable. Therefore, numerical methods are in many cases used to solve the equations and achieve solutions for the flow over the disk. The boundary layer flow over a revolving disk has some fascinating features such as the disk rotates faster, the thickness of the boundary layer decreases. Certainly, particular rotational speed, the boundary layer turn into a very thin, and the flow convert from a turbulent flow to a laminar one that critical rotational speed is also called the critical Reynold's number, and it is based on the viscosity and density of the fluid, besides the diameter and rotational speed of the disk. The boundary layer flow over a rotating disk has many practical applications, including the design of turbine blades, cooling of electronic components, and manufacturing of flat panel displays. Understanding the behavior of the surface layer flow over a swirling disk is therefore have a great importance for the optimization of these applications.

Non-Newtonian and Newtonian fluids have significant impact in accordance with the plate-cone rheometry. By using the finite element method, Kumar et al. [12] explored the entropy creation of a nanoliquid made of nanoscale copper and aluminium oxide particles between the gaps of two coaxial rotating discs. The heat flux on the two coaxial stretchable spinning discs along two carbon nano tubes (CNT) nanoliquids was modelled by Bhattacharyya et al. [13]. Hafeez et al. [14] recently looked at the fluid flow over a rotating disc. With the aid of Fortran code, Nazari et al. [15], explored the H_2O/Al_2O_3 nanoliquid numerically with 0 to 4% motion of nanosized particles driven by cold and hot lids in a two-dimensional square cavity. Ahmed et al. [16] dissected the impact of heat conduction and homogeneous-heterogeneous reactions on the Maxwell equation between two revolving discs.

Shear stress in a non-Newtonian fluid called a Casson fluid is not linearly proportional to velocity gradients. There are wide spread engineering applications for the study of the Casson fluid. With numerous uses in bio-mechanics, polymers and metals, the Casson fluid is one of the most substantial non-Newtonian fluid. The nonlinear Casson integral equation, which was developed by Casson [17], describes the stress and strain rate have a link by constructing a complex function that integrates the complex domain equation for momentum and energy and is manifestly crucial for temperature fields, velocity and the Helmholtz wave equation. Walawender et al. [18] explored at a blood tube model for the Casson fluid, where the volumetric flow rate and pressure decreases were estimated by experimentation. An analysis for a high Dean number was conducted by Batra and Jena [19] on a constant continuous flow of a Casson fluid in a rounded top cylindrically-shaped tube. The Casson fluid contains gyrotactic microorganisms and flows through a multilayer tensile

cylinder which was proposed by Dawar et al. [20]. Shaheen et al. [21] investigated how different characteristics of a elastic cylinder enclosed in a porous material to alter the electrically conductive, two-dimensional, radiative, Casson nano liquid flow together combining chemical and kinetic reaction and activation energy.

Highly nonlinear boundary value problems are faced by automotive industry now a days. Convergence is attuned to the starting framework and tranquility constants for a large class of problems that are frequently treated by other arithmetical techniques. The PCM's objective is to show how widely applicable the technique is as a workable remedy for nonlinear problems as discussed by Patil [22]. According to Shuaib et al. [23], who highlighted the surface-to-surface heat transfer and 3D turbulent flow across an extended spinning disc. In the existence of strong exterior magnetic fields, the fluid flow was explored. Engineering disciplines must consistently dealt with complex systems which was examined by Wang et al. [24] by using a parameter variation technique. They also noticed at the stationary splitting that happens when nonlinear initial value problems with various features are solved and they created a method for pinpointing the precise locations of the bifurcation points. A stretched cylinder that was being guided by suction/injection impact was the object of investigation done by Bilal et al. [25]. Many researchers worked on aforementioned ingredients of the flow models like [26–38].

The computational behavior of trihybrid nanofluid flow inside a cone and rotating disk differs significantly from hybrid nanofluid flow due to the additional complexity introduced by the trihybrid system. The trihybrid nanofluid incorporates three distinct types of nanoparticles, leading to intricate fluid dynamics and thermal interactions. This complexity results in a more intricate computational model, requiring advanced numerical methods and increased computational resources. The interaction between the cone and rotating disk further amplifies the challenges, as the trihybrid nanofluid experiences diverse flow patterns and heat transfer characteristics. Understanding and simulating these intricate phenomena are crucial for optimizing the performance of systems involving trihybrid nanofluids within cone and rotating disk configurations. According to the research indicated above, no attempt has been made to date to investigate the disc and cone tri-hybrid nanofluid flow model as moving or stationary when subjected to magnetic field. This study examines how Al_2O_3 , TiO_2 and Ag nanoparticles play a role in the thermophysical characteristics of blood. It has numerous significant uses in science and technology. Developing a mathematical model for spinning cone and disc, which rotate both in unison and in opposition whether they are stationary or in motion, is the next important step. Then by using shooting method, the coupled equations are reduced to an ordinary system. The impacts of different rheological parameters embedded in the system are noticed through graphs. Most possible cases of the different schemes between the cone and rotating disk are evaluated. We considered trihybrid nanofluid model which is more effective in the enhancement of heat transfer and thermal conductivity of the fluid as compared to hybrid nanofluid models.

The following queries while the discussion of the problem are raised:

- How can the study results be applied to enhance industrial processes using trihybrid Casson nanofluids?
- How can the study results be applied to enhance industrial processes using trihybrid Casson nanofluids?
- What are the key objectives of studying trihybrid Casson nanofluid computational behavior?
- How do the study results align with or differ from previous research on hybrid nanofluids?

2. Mathematical modeling

Suppose a cone and disk with an incompressible trihybrid nanofluid while taking magnetic field for blood flow influence into account. Figures 1(a-c) show the geometry of the problem, where Figure 1(a) presents the actual model of cone and disk, Figure 1(b) shows the graphical model of cone and disk, and Figure 1(c) depicts the geometry of the model. The tools (disk and cone) are taken to be stationary or revolving with a rotational frequency in the cylindrical coordinates (r, ϕ, z) . The Ω and ω emphasize the disk and cone rotational frequency respectively. In contrast to the induced magnetic field, which is ignored, B_0 measures the magnetical field's intensity is applied in the z -direction. The viscous dissipation is added to the computation of heat transportation modelling. This occurrence is effectively used to radially changing wall temperature $T_w = T_\infty + cr^n$, on the exterior of the disk where c and n are kept fixed and cone wall temperature of the disk is T_∞ . P is the pressure inside the conical gap and is influenced by both axial z and the radial r extents [39, 40].

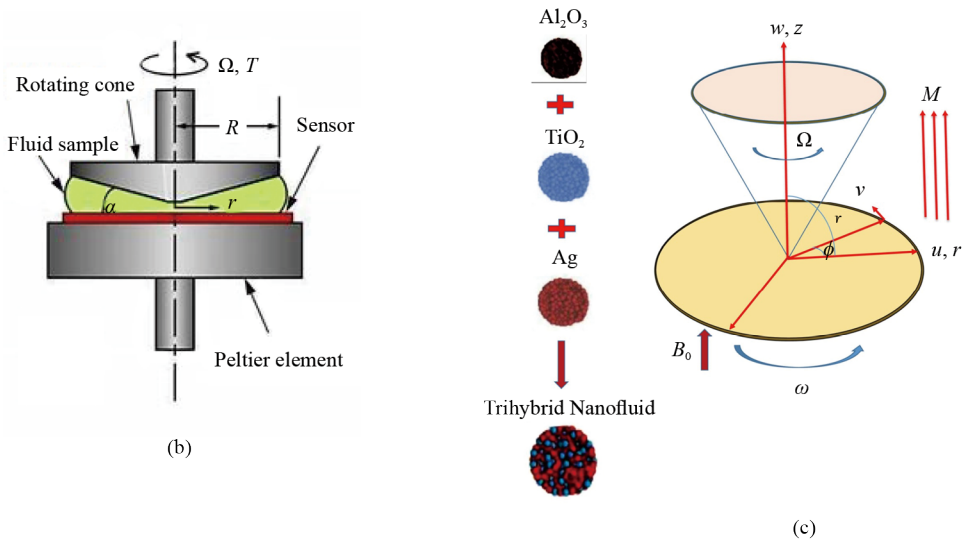
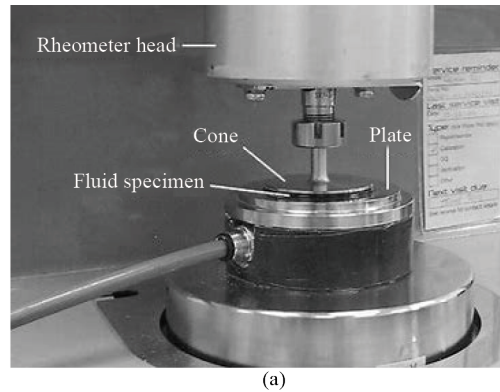


Figure 1. Graphical and actual models of cone and disk [41]

$$\frac{u}{r} + \frac{\partial w}{\partial z} + \frac{\partial u}{\partial r} = 0, \quad (1)$$

$$\left[-\frac{v^2}{r} + w \frac{\partial u}{\partial z} + u \frac{\partial u}{\partial r} \right] \rho_{thnf} = \left(\frac{1+\beta}{\beta} \right) \mu_{thnf} \left[\frac{1}{r} \frac{\partial u}{\partial r} + \frac{\partial^2 u}{\partial z^2} + \frac{\partial^2 u}{\partial r^2} - \frac{u}{r^2} \right] - \frac{\partial p}{\partial r} - \sigma_{thnf} B_0^2 u, \quad (2)$$

$$\rho_{thnf} \left[u \frac{\partial v}{\partial r} + w \frac{\partial v}{\partial z} + \frac{uv}{r} \right] = \left(\frac{\beta+1}{\beta} \right) \mu_{thnf} \left[\frac{\partial^2 v}{\partial r^2} + \frac{\partial^2 v}{\partial z^2} + \frac{1}{r} \frac{\partial v}{\partial r} - \frac{v}{r^2} \right] - \sigma_{thnf} B_0^2 v, \quad (3)$$

$$\rho_{thnf} \left[w \frac{\partial w}{\partial z} + u \frac{\partial w}{\partial r} \right] = \left(\frac{1+\beta}{\beta} \right) \mu_{thnf} \left[\frac{\partial^2 w}{\partial z^2} + \frac{1}{r} \frac{\partial w}{\partial r} + \frac{\partial^2 w}{\partial r^2} \right] - \frac{\partial p}{\partial z}, \quad (4)$$

$$\left[w \frac{\partial T}{\partial z} + u \frac{\partial T}{\partial r} \right] (\rho c p)_{thnf} = \sigma_{thnf} B_0^2 (u^2 + v^2) + k_{thnf} \frac{\partial^2 T}{\partial z^2}. \quad (5)$$

Where p is the fluid pressure and (u, v, w) are the velocity components along (r, ϕ, z) directions, B_0 is the magnetic strength, while, k_{thnf} , ρ_{thnf} , ν_{thnf} , μ_{thnf} , $(\rho C_p)_{thnf}$ and σ_{thnf} are the thermal conductivity, density, kinematic viscosity, dynamic viscosity, specific heat and electric conductivity regarding to trihybrid nanoliquid's in the order mentioned.

The necessary boundary values are as [39]:

$$u = 0, v = \omega r, w = 0, T = T_w \quad \text{at} \quad z = 0, \quad (6)$$

$$u = 0, v = \Omega r, w = 0, T = T_\infty \quad \text{at} \quad z = r \tan \gamma. \quad (7)$$

The vertex between the cone and disk is here specified by γ . The expression $(v = \omega r)$ evaluated at $(z = 0)$ implies rotational motion along the disk, while $(v = \Omega r)$ at $(z \rightarrow r \tan \gamma)$ signifies rotation along the cone, indicating the presence of a cylindrical coordinate system. These conditions, when combined with the absence of a pressure gradient, suggest a fluid state where no external forces are driving the motion. Furthermore, the maintenance of constant temperature in this context implies an isothermal process, where the fluid experiences no change in temperature as it undergoes these rotational movements. This scenario is characteristic of a system governed by fluid dynamics, specifically in cylindrical coordinates, and sheds light on the equilibrium state of the fluid in the absence of external influences. The expressions $(v = \omega r)$ and $(v = \Omega r)$ serve as crucial indicators of the rotational behavior within this system, allowing for a detailed analysis of the fluid's motion along both the disk and the cone.

Similarity conversions: We used the following similarity transformation to achieve non-dimensionalization [39]:

$$u = \frac{v_f F(\eta)}{r} = U_w F(\eta), v = \frac{v_f G(\eta)}{r} = U_w G(\eta), w = \frac{v_f H(\eta)}{r} = U_w H(\eta), p = \frac{\rho v_f^2 P}{r^2} U_w^2 \rho \cdot p, \\ \eta = \frac{z}{r}, \theta = \frac{T - T_\infty}{T_w - T_\infty}, M = \frac{v_f \sigma_f B_0^2}{\rho_f U_w^2}, Pr = \frac{\mu_f C_p}{k_f}. \quad (8)$$

Here, the magnetic field, M , the surface velocity, and the Prandtl number are all employed. Now the modelled Eqs. (1-5) have undergone these modifications as described in Eqs. (6) and (7), the changes to their boundary conditions are seen. The translation of Equations (2) to (5) results from the previous conversion into the non-dimensional given by:

$$H' - \eta F' = 0, \quad (9)$$

$$\left(\frac{1+\beta}{\beta}\right)(1+\eta^2)F'' + 3\eta F' + (1-\phi_1)^{2.5}(1-\phi_2)^{2.5}(1-\phi_3)^{2.5} \\ \left[(1-\phi_1)\left((1-\phi_2)\left\{(1-\phi_3) + \frac{\rho_3}{\rho_f}\phi_3\right\} + \frac{\rho_2}{\rho_f}\phi_2\right) + \frac{\rho_1}{\rho_f}\phi_1\right][\eta FF' - HF' + F^2 - G^2] \\ + (1-\phi_1)^{2.5}(1-\phi_2)^{2.5}(1-\phi_3)^{2.5}[2p + \eta p' - MF] = 0, \quad (10)$$

$$\begin{aligned} & \left(\frac{1+\beta}{\beta}\right)(1+\eta^2)G'' + 3\eta G' - (1-\phi_1)^{2.5}(1-\phi_2)^{2.5}(1-\phi_3)^{2.5} \\ & \left[(1-\phi_1) \left((1-\phi_2) \left\{ (1-\phi_3) + \frac{\rho_3}{\rho_f} \phi_3 \right\} + \frac{\rho_2}{\rho_f} \phi_2 \right) + \frac{\rho_1}{\rho_f} \phi_1 \right] [\eta FG' - HG'] \\ & - (1-\phi_1)^{2.5}(1-\phi_2)^{2.5}(1-\phi_3)^{2.5} MG = 0, \end{aligned} \quad (11)$$

$$\begin{aligned} & \left(\frac{1+\beta}{\beta}\right)(1+\eta^2)H'' + 3\eta H' + (1-\phi_1)^{2.5}(1-\phi_2)^{2.5}(1-\phi_3)^{2.5} \\ & \left[(1-\phi_1) \left((1-\phi_2) \left\{ (1-\phi_3) + \frac{\rho_3}{\rho_f} \phi_3 \right\} + \frac{\rho_2}{\rho_f} \phi_2 \right) + \frac{\rho_1}{\rho_f} \phi_1 \right] [\eta FH' - HH' + H + FH] \\ & - (1-\phi_1)^{2.5}(1-\phi_2)^{2.5}(1-\phi_3)^{2.5} p' = 0, \end{aligned} \quad (12)$$

$$\begin{aligned} & \left\{ \frac{1-\phi_3 + 2\phi_3 \left(\frac{k_1}{k_1 - k_{hnf}} \right) \ln \frac{k_1 + k_{hnf}}{2k_{hnf}}}{1-\phi_3 + 2\phi_3 \left(\frac{k_{hnf}}{k_1 - k_{hnf}} \right) \ln \frac{k_1 + k_{hnf}}{2k_{hnf}}} \right\} \left\{ \frac{1-\phi_2 + 2\phi_2 \left(\frac{k_2}{k_2 - k_{nf}} \right) \ln \frac{k_2 + k_{nf}}{2k_{nf}}}{1-\phi_2 + 2\phi_2 \left(\frac{k_{nf}}{k_2 - k_{nf}} \right) \ln \frac{k_2 + k_{nf}}{2k_{nf}}} \right\} \\ & \left\{ \frac{1-\phi_1 + 2\phi_1 \left(\frac{k_3}{k_3 - k_f} \right) \ln \frac{k_3 + k_f}{2k_f}}{1-\phi_1 + 2\phi_1 \left(\frac{k_f}{k_3 - k_f} \right) \ln \frac{k_3 + k_f}{2k_f}} \right\} \left((1+\eta^2)\theta'' + \eta(1-2n)\theta' + n^2\theta \right) \\ & + Pr \left[(1-\phi_1) \left((1-\phi_2) \left[(1-\phi_3) + \frac{(\rho C_p)_3}{(\rho C_p)_f} \phi_3 \right] + \frac{(\rho C_p)_2}{(\rho C_p)_f} \phi_2 \right) + \frac{(\rho C_p)_1}{(\rho C_p)_f} \phi_1 \right] \\ & [\eta F\theta' - nF\theta - H\theta'] + (F^2 + G^2) \frac{M}{(1-\phi_1)^{2.5}(1-\phi_2)^{2.5}(1-\phi_3)^{2.5}} = 0. \end{aligned} \quad (13)$$

The altered condition are:

$$H(0) = F(0) = 0, G(0) = Re_\omega, \theta(0) = 1, \quad (14)$$

$$F(\eta_o) = H(\eta_o) = 0, G(\eta_o) = Re_\omega, \theta(\eta_o) = 0.$$

Al_2O_3 , TiO_2 and Ag are used to illustrate the volumetric fraction of these three materials. While k_{tnf} is trihybrid water-nanoliquid's heat conductivity.

Heat-related characteristics: The varied thermal characteristics of blood and hybrid nanoliquids are listed below.

$$\begin{aligned} \mu_{thnf} &= \frac{\mu_f}{(1-\phi_1)^{2.5}(1-\phi_2)^{2.5}(1-\phi_3)^{2.5}}, \\ \rho_{thnf} &= \left[(1-\phi_1) \left((1-\phi_2)[(1-\phi_3)\rho_f + \rho_3\phi_3] + \rho_2\phi_2 \right) + \rho_1\phi_1 \right], \\ (\rho C_p)_{thnf} &= (1-\phi_1) \left((1-\phi_2)[(1-\phi_3)(\rho C_p)_f + (\rho C_p)_{s3}\phi_3] + (\rho C_p)_{s2}\phi_2 \right) + (\rho C_p)_{s1}\phi_1. \end{aligned} \quad (15)$$

The tri-hybrid Xue model is given by

$$\begin{aligned} \frac{k_{thnf}}{k_{nf}} &= \frac{1-\phi_3 + 2\phi_3 \left(\frac{k_1}{k_1 - k_{thnf}} \right) \ln \frac{k_1 + k_{thnf}}{2k_{thnf}}}{1-\phi_3 + 2\phi_3 \left(\frac{k_{thnf}}{k_1 - k_{thnf}} \right) \ln \frac{k_1 + k_{thnf}}{2k_{thnf}}}, \\ \frac{k_{thnf}}{k_{nf}} &= \frac{1-\phi_2 + 2\phi_2 \left(\frac{k_2}{k_2 - k_{thnf}} \right) \ln \frac{k_2 + k_{thnf}}{2k_{thnf}}}{1-\phi_2 + 2\phi_2 \left(\frac{k_{thnf}}{k_2 - k_{thnf}} \right) \ln \frac{k_2 + k_{thnf}}{2k_{thnf}}}, \\ \frac{k_{thnf}}{k_f} &= \frac{1-\phi_1 + 2\phi_1 \left(\frac{k_3}{k_3 - k_f} \right) \ln \frac{k_3 + k_f}{2k_f}}{1-\phi_1 + 2\phi_1 \left(\frac{k_f}{k_3 - k_f} \right) \ln \frac{k_3 + k_f}{2k_f}}. \end{aligned} \quad (16)$$

3. Numerical solution

Introducing dependent quantities $y_1, y_2, y_3, y_4, y_5, y_6, y_7, y_8$ and y_9 such that

$$\begin{aligned} F &= y(1), F' = y(2), F'' = y(2)', G = y(3), G' = y(4), G'' = y(4)', H = y(5), \\ H' &= y(6), H'' = y(6)', P = y(7), \theta = y(8), \theta' = y(9), \theta'' = y(9)'. \end{aligned} \quad (17)$$

$$\begin{aligned} y_2' &= -3\eta y_2 - (1-\phi_1)^{2.5}(1-\phi_2)^{2.5}(1-\phi_3)^{2.5} \\ &\times \left[(1-\phi_1) \left((1-\phi_2)[(1-\phi_3)\rho_f + \rho_3\phi_3] + \rho_2\phi_2 \right) + \rho_1\phi_1 \right] [\eta y_2 y_1 - y_5 y_2 + y_1^2 - y_5^2] \\ &- (1-\phi_1)^{2.5}(1-\phi_2)^{2.5}(1-\phi_3)^{2.5} [2p + \eta p' - M y_1] \times \left(\frac{1}{(1+\eta^2)} \right) \times \left(\frac{\beta}{(1+\beta)} \right), \end{aligned} \quad (18)$$

$$\begin{aligned}
y_4' &= -3\eta y_4 - (1 - \phi_1)^{2.5}(1 - \phi_2)^{2.5}(1 - \phi_3)^{2.5} \\
&\times \left[(1 - \phi_1) \left((1 - \phi_2) [(1 - \phi_3)\rho_f + \rho_3\phi_3] + \rho_2\phi_2 \right) + \rho_1\phi_1 \right] [\eta y_1 y_4 - y_5 y_4] \\
&- (1 - \phi_1)^{2.5}(1 - \phi_2)^{2.5}(1 - \phi_3)^{2.5} \times \left(\frac{1}{(1 + \eta^2)} \right) \times \left(\frac{\beta}{(1 + \beta)} \right), \tag{19}
\end{aligned}$$

$$\begin{aligned}
y_6' &= -3\eta y_6 - (1 - \phi_1)^{2.5}(1 - \phi_2)^{2.5}(1 - \phi_3)^{2.5} \\
&\times \left[(1 - \phi_1) \left((1 - \phi_2) [(1 - \phi_3)\rho_f + \rho_3\phi_3] + \rho_2\phi_2 \right) + \rho_1\phi_1 \right] [\eta y_1 y_6 - y_5 y_6 + y_5 + y_1 y_5] \\
&- (1 - \phi_1)^{2.5}(1 - \phi_2)^{2.5}(1 - \phi_3)^{2.5} p' \times \left(\frac{1}{(1 + \eta^2)} \right) \times \left(\frac{\beta}{(1 + \beta)} \right), \tag{20}
\end{aligned}$$

$$\begin{aligned}
y_9' &= -[\eta(1 - 2n)y_9 + (n^2)y_8] - \left(\frac{k_{hnf}}{k_{t,hnf}} \right) \times \\
&\left(Pr \left[(1 - \phi_1) \left((1 - \phi_2) \left[(1 - \phi_3) + \frac{(\rho C_p)_{s_3}}{(\rho C_p)_f} \phi_3 \right] + \frac{(\rho C_p)_{s_2}}{(\rho C_p)_f} \phi_2 \right) + \frac{(\rho C_p)_{s_1}}{(\rho C_p)_f} \phi_1 \right] \right. \\
&\left. [\eta y_1 y_9 - n y_1 y_8 - y_5 y_9] + (y_1^2 + y_3^2) \frac{M}{(1 - \phi_1)^{2.5}(1 - \phi_2)^{2.5}(1 - \phi_3)^{2.5}} \right) \times \left(\frac{1}{(1 + \eta^2)} \right). \tag{21}
\end{aligned}$$

Every numerical solutions are obtained by putting $\varepsilon = 10^{-5}$ where ε is defined as tolerance.

4. Result and discussion

This section includes the discussion of Figures and Tables. Figures 2 and 3 show the rheological flow patterns and mathematical layout of the problem while Figures 4-36 show the influence of emerging rheological parameters on velocity and temperature profiles. The link between the axial velocity profile $F(\eta)$ and the magnetic number (M) is seen in Figure 4. The fluid velocity of the trihybrid nanoliquids containing Al_2O_3 , TiO_2 , and Ag decreases with an increment in the magnetic parameter. The Lorentz force, which slows the flow velocity and is produced by the magnetic number M , can be used to explain this occurrence. The effect of volume fraction parameters Al_2O_3 , TiO_2 , and Ag on the axial velocity profile $F(\eta)$ is shown in Figures 5, 6 and 7. The axial velocity profile positively decreases as the volume fractions of Al_2O_3 , TiO_2 , and Ag increases. The velocity profile as a whole decreases as a result of the volume fractions being enhanced, which also thickens the boundary layer. Figure 5 enables the volume fraction in accordance with the Al_2O_3 versus velocity profile, as with an elevation in the intensity of the nanoparticles, the viscosity of the nanofluid becomes more which appears as a resistive force and that's why velocity turns down at large. Figure 6 renders the volume fraction of nanoparticles embedded with TiO_2 for velocity profile which shows subside behavior due to the intensity of the nanoparticles. Figure 7 portrays the

volume fraction of nanoparticles embedded with Ag for velocity distribution which reduces the velocity component, due to vigorous nature of the nanoparticles merged into fluid.

Higher levels of rotation for the cone and disc show a significant rise in the velocity profile $F(\eta)$, as seen in Figures 8 and 9. The reason for this increase is that the devices with Re_Ω and Re_ω have higher angular velocities, which cause the fluid particles to travel more quickly. As a result, the axial velocities $F(\eta)$ throughout the disk and cone become inclined. As the Casson parameter (β) decreases, the axial velocity increases (Figure 10), which solely takes into account the rotating cone/stationary disk situation. Physically speaking, this makes sense because the Casson parameter causes the fluid's viscosity to decrease, increasing the fluid's total velocity.

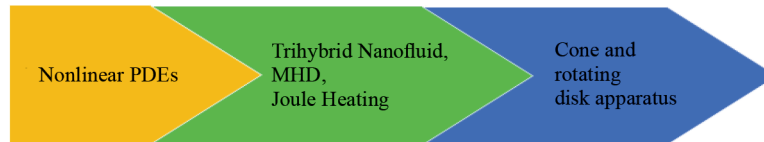


Figure 2. Rheological flow pattern



Figure 3. Mathematical modeling layout

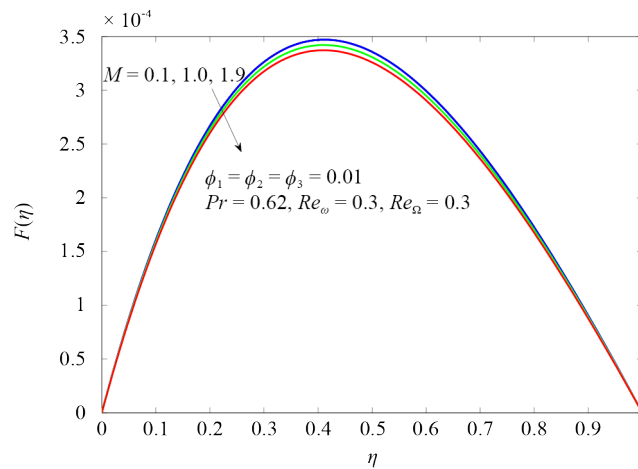


Figure 4. The consequence of M against $F(\eta)$

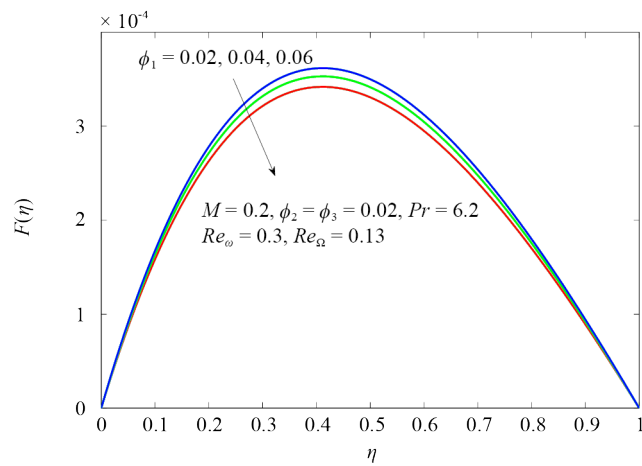


Figure 5. The ramification of ϕ_1 against $F(\eta)$

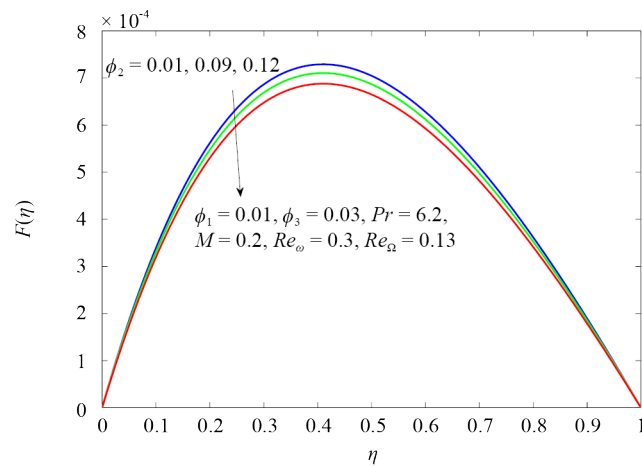


Figure 6. The consequence of ϕ_2 against $F(\eta)$

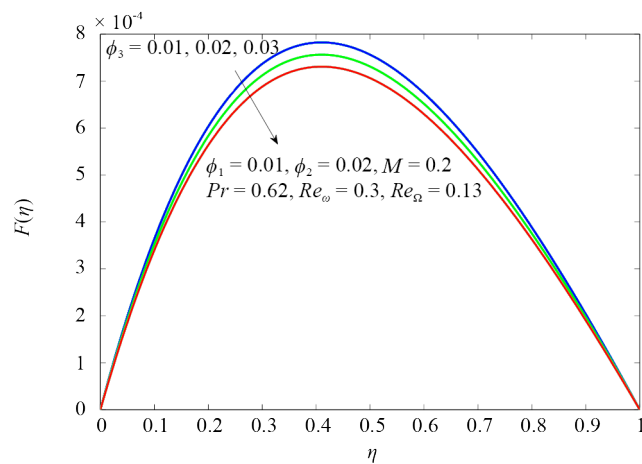


Figure 7. The consequence of ϕ_3 against $F(\eta)$

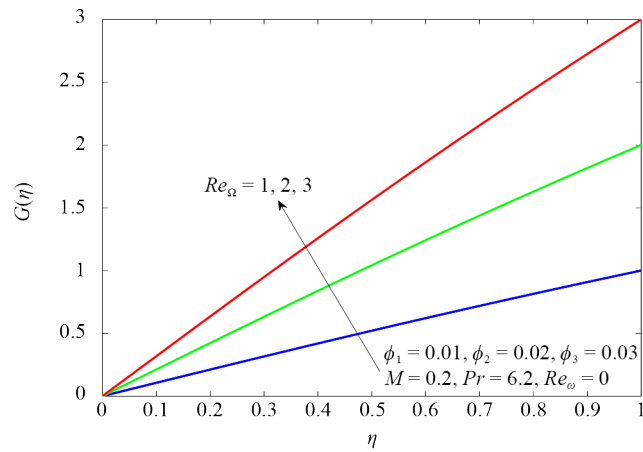


Figure 8. The consequence of Re_{Ω} against $F(\eta)$

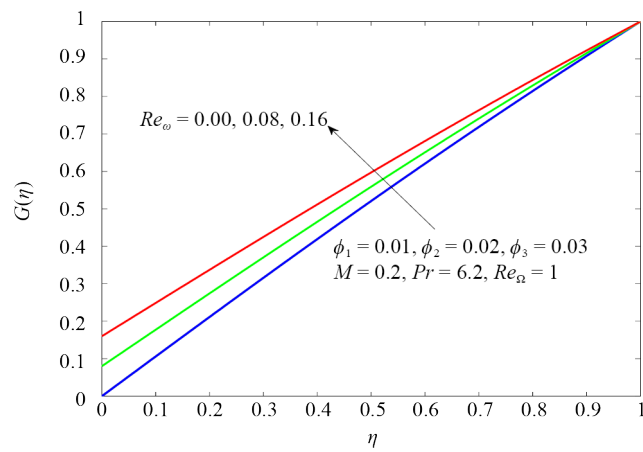


Figure 9. The consequence of Re_{ω} against $F(\eta)$

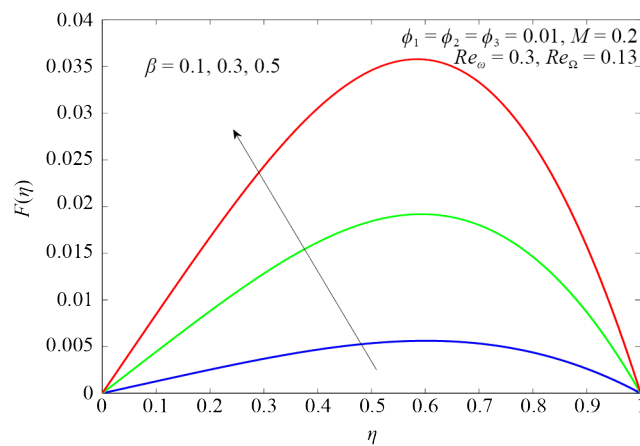


Figure 10. The consequence of β against $F(\eta)$

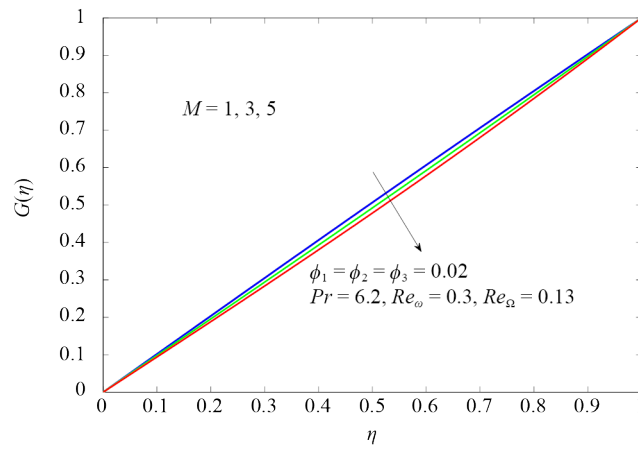


Figure 11. The consequence of M against $F(\eta)$

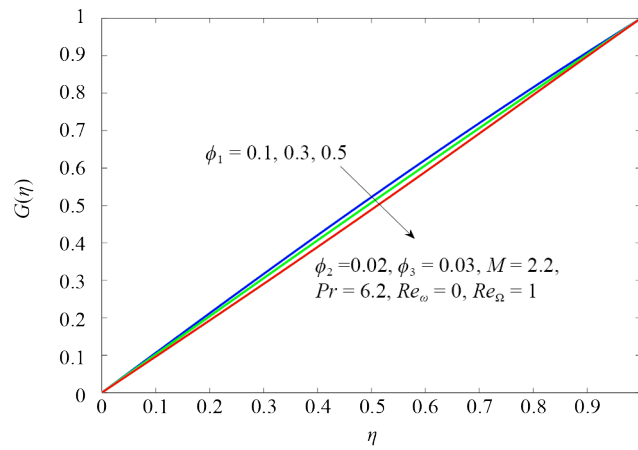


Figure 12. The ramification of ϕ_1 against $G(\eta)$

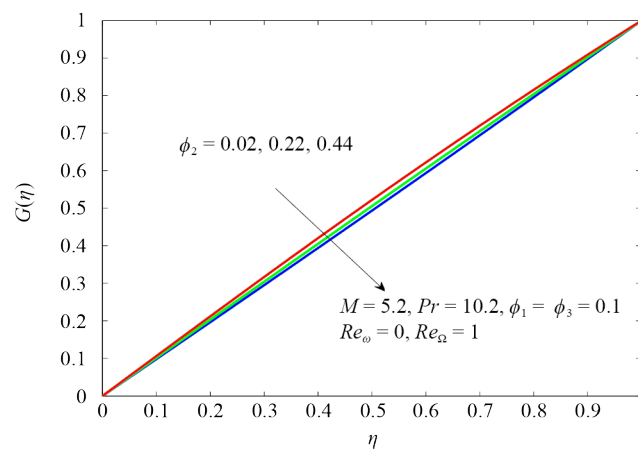


Figure 13. The ramification of ϕ_2 against $G(\eta)$

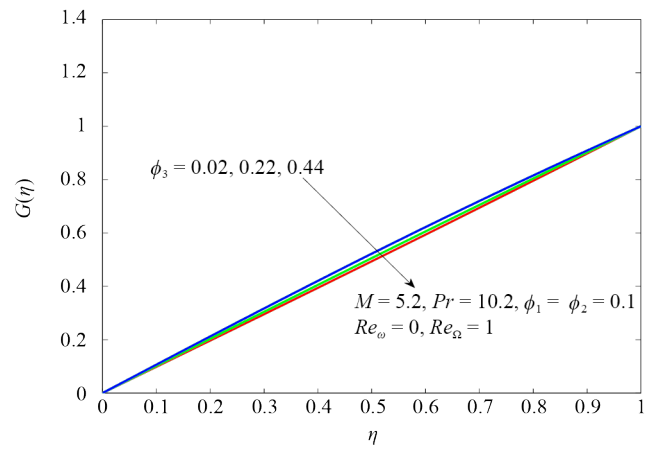


Figure 14. The ramification of ϕ_3 against $G(\eta)$

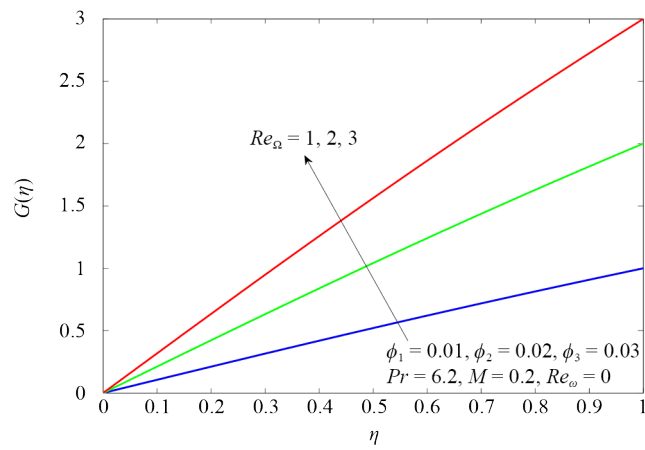


Figure 15. The consequence of Re_{Ω} against $G(\eta)$

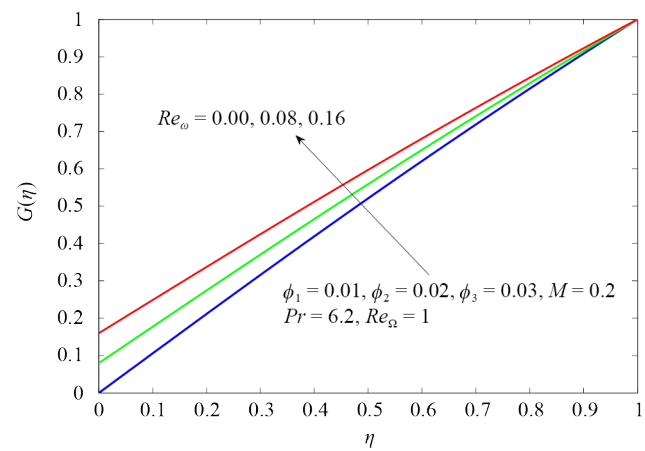


Figure 16. The consequence of Re_{ω} against $G(\eta)$

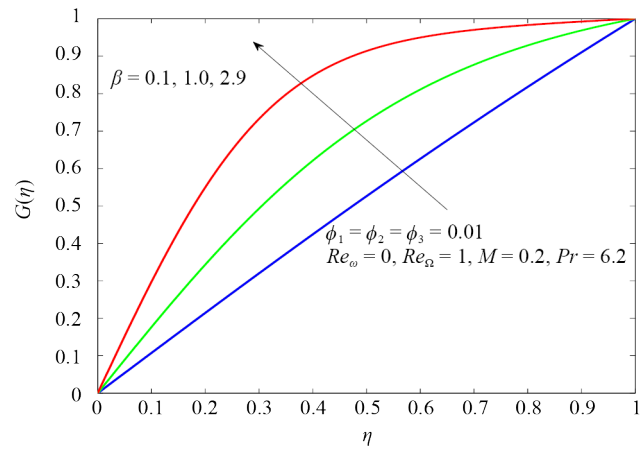


Figure 17. The consequence of β against $G(\eta)$

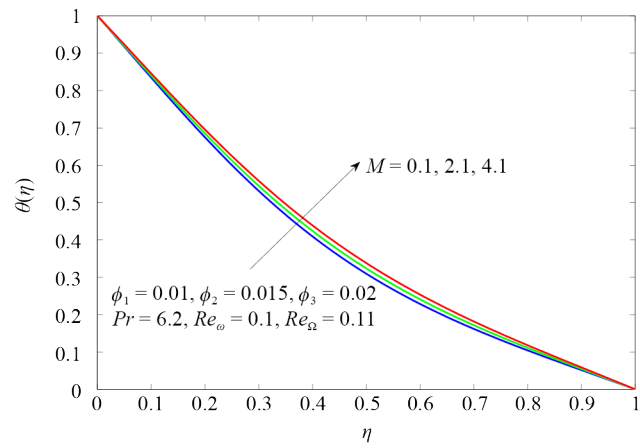


Figure 18. The consequence of M against $\theta(\eta)$

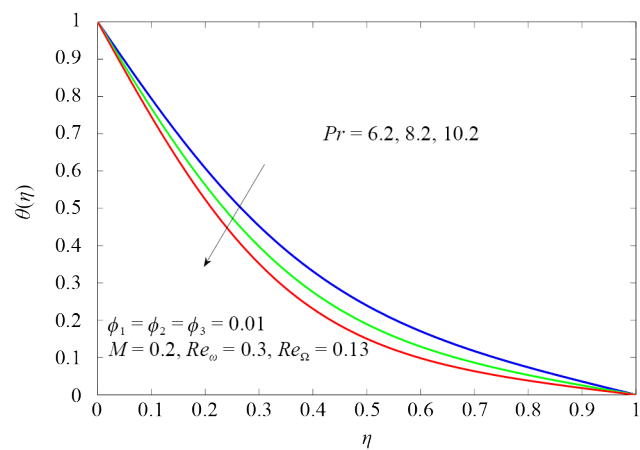


Figure 19. The Impression of Pr against $\theta(\eta)$

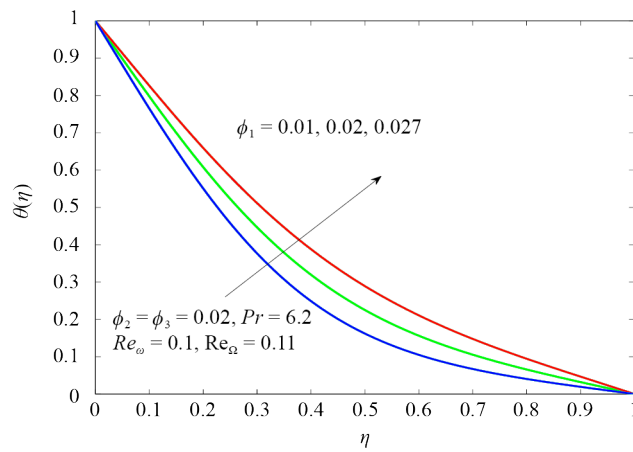


Figure 20. The repercussion of ϕ_1 against $\theta(\eta)$

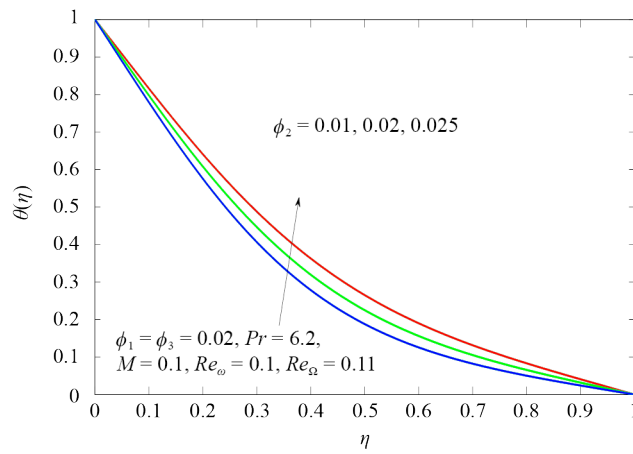


Figure 21. The repercussion of ϕ_2 against $\theta(\eta)$

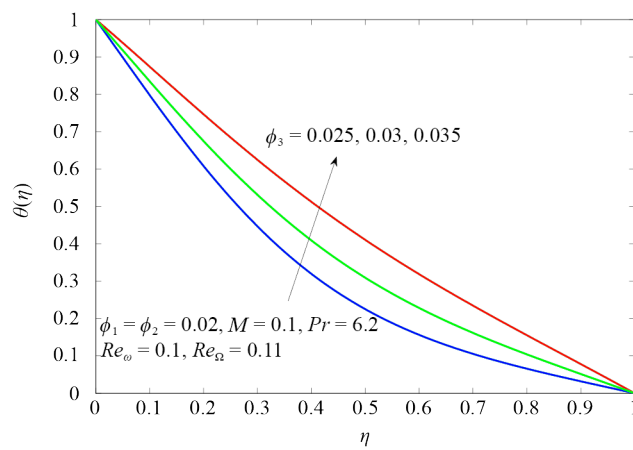


Figure 22. The consequence of ϕ_3 against $\theta(\eta)$

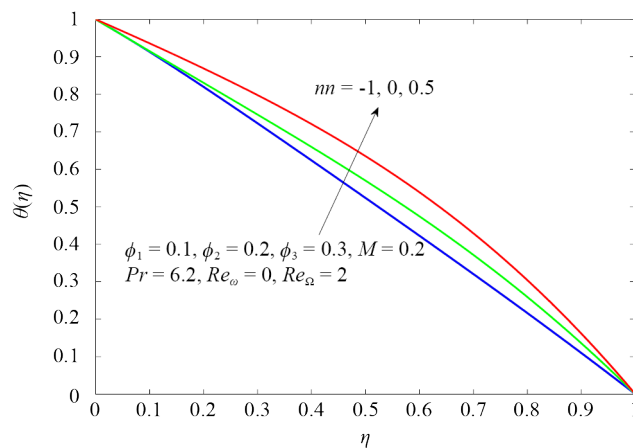


Figure 23. At three distinct radial exponents, the influence of $\theta(\eta)$ between a static disk and revolving cone

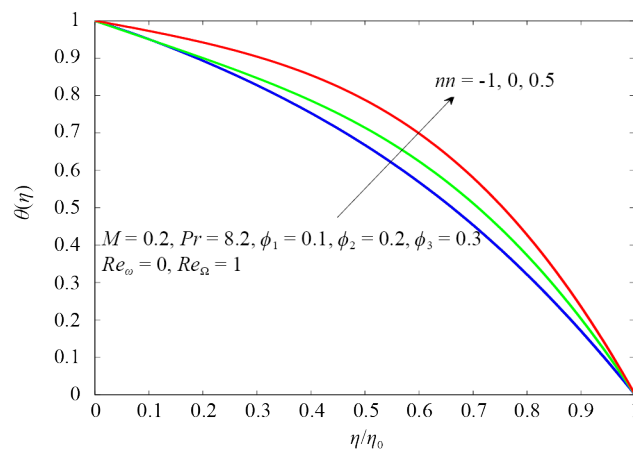


Figure 24. At three distinct radial exponents, the influence of $\theta(\eta)$ between a static disk and revolving cone

A detailed analysis of the impact of several parameters on the radial velocity profile $G(\eta)$ is shown in Figures 11, 12, 13, and 14. These parameters include the magnetic parameter (M) and the volume ratios of aluminum oxide (Al_2O_3), titanium dioxide (TiO_2), and silver (Ag). We can see from these images the complex interactions between these factors and how they affect radial velocity. It is clear by examining the magnetic parameter (M), as shown in Figure 11, that the behavior of the radial velocity profile $G(\eta)$ is comparable to that of the previously stated axial velocity profile. The radial velocity of the trihybrid nanoliquids containing Al_2O_3 , TiO_2 , and Ag decreases with a reduction in the magnetic parameter. The magnetic field's Lorentz force is responsible for this decrease in radial velocity. In particular, the volume ratio factors of Al_2O_3 , TiO_2 and Ag, respectively, are the subject of Figures 12, 13, and 14. A drop in these nanoparticles' volume fractions is correlated with a decrease in radial velocity, much like the axial velocity profile. This phenomenon is explained by the way that lower volume fractions thicken the boundary layer, which in turn lowers the radial velocity overall. Figure 12 renders the volume fraction of nanoparticles embedded with Al_2O_3 for momentum distribution profile $G(\eta)$ which shows subsidence behavior due to the intensity of the nanoparticles. Figure 13 portrays the volume fraction of nanoparticles embedded with TiO_2 for momentum distribution $G(\eta)$ which reduces the velocity component, due to vigorous nature of the nanoparticles merged into fluid. Figure 14 enables the volume fraction in accordance with Ag versus momentum profile $G(\eta)$, as with an elevation in the intensity of the nanoparticles, the viscosity of the nanofluid becomes more which appears as a resistive force and that's why velocity turns down at large. Figure 15 displays the

significance of Re_{Ω} on the dimensionless velocity $G(\eta)$ the gain in the value of Re_{Ω} enriches the $G(\eta)$ when $Re_{\omega} = 0$. The rate of inclination of $G(\eta)$ significantly increases with increasing values of Re_{Ω} . Figure 16 displays the significance of Re_{ω} on the dimensionless momentum profile $G(\eta)$. Raising the values of Re_{ω} enriches the $G(\eta)$ when $Re_{\Omega} = 1$. The rate of inclination of $G(\eta)$ significantly increases with increasing values Re_{ω} . Moreover, the rate of inclination in the velocity profile is faster for the fluid flow without aggregation effect than the others. The radial velocity increased as discussed in the Figure 17 when parameter (β) is raised, as can be seen from this figure. Physically, the parameter raises the fluid velocity by measuring the additional viscosity of the fluid.

Figure 18 describes the nature of the relationship between temperature distribution $\theta(\eta)$ and magnetic field strength M . The Lorentz force prevents the fluid from moving, which causes some heat to be produced, it finally causes $\theta(\eta)$ temperature of fluid to increase. In Figure 19, it is evident that the Prandtl number Pr predominates when compared to the temperature distribution. Physically, thermal diffusivity is always lower for large Prandtl fluxes than for low Prandtl fluxes by including more nanoparticles of Al_2O_3 , TiO_2 and Ag , the fluid temperature in Figures 20, 21, and 22 is described as a result of a rise in the carrier fluid's viscosity and capacity to absorb heat. Throughout the computational effort, we rigorously fixed Reynold's numbers 0 and 1. The Reynold's number is multiplied by 1.01 in the case of co-rotation and by -1 in the case of counter-rotation. We only restrict the power index values $n = -1, 0, 0.05$. The model suggests that it can be changed while depending on the circumstances. Here, cases 1 and 2 represents a stationary disc and rotating cone, whereas cases 3 and 4 represents a co-rotating cone and disc, and case 4 a stationary cone and rotating disc when the disc and cone are both rotating anticlockwise. In order to discuss the similarities in temperature, Figures 23, 24 are sketched. Between a still disc and a turning cone (case 1), depending on the credit given to (Re_{ω}) using scenario 1. Conical space between the cone's and disc's surfaces, temperature field is depicted. It is evident that the temperature is marginally affected by the thermal layer which increase in all directions at regular apex angles. Although there is little effect when the gap angle is small. The fluid at the surface of disk becomes an insulating layer when the critical power index approaches values of $n = -1, 0, 0.05$, which completely eliminates heat transfer from the disc surface.

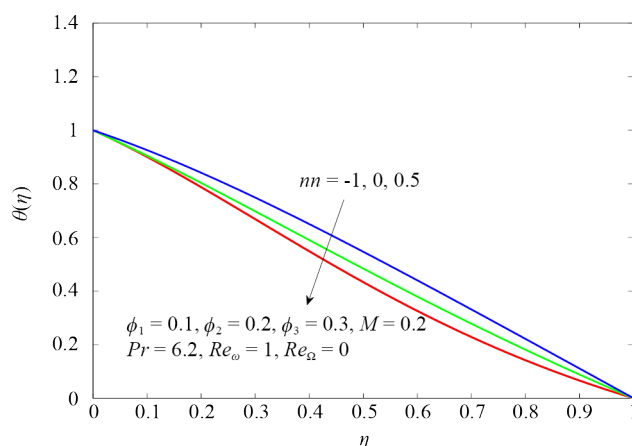


Figure 25. Between a stationary cone and a moving disc, an impression of $\theta(\eta)$ at three different radial exponents

In Case 2, which involves a stationary cone and a revolving disc, Figures 25 and 26 depict the temperature distribution and heat transfer occurring within the conical gap between the disc and the cone surface. As it can be observed, example 2 only experiences a high rate of heat transfer at fixed wall temperatures ($n = 0$). However, given a wide range of radially varying disc temperature distribution, a stationary cone and revolving disc encounter an accelerated cooling process. Case 3 (the scenario with the co-rotating disc and cone) is summarised in Figures 27 and 28. The system's temperature rapidly drops with the co-rotation of the disc and cone, it is inferred last but not least, illustrates instance 4 (both disc and cone are counter rotating) mentioned in Figures 29 and 30. It is determined that the system's temperature rapidly drops with the disc and cone rotating in tandem. The heat generated there is what causes the temperature to rise when the cone and

disc are rotating counter to one another since this provides retardation forces that prevent the gas particles from moving. As seen in Figures 29 and 30, the thermal profile $\theta(\eta)$ considerably rises with increasing values for the rotation of the cone and disc. Physically, the faster fluid particles move due to the increased angular velocities of both Re_Ω and Re_ω devices, which causes an inclination in the energy $\theta(\eta)$ across the disk and cone. Figure 31 displays the significance of Re_Ω on the dimensionless $\theta(\eta)$ the gain the value of Re_Ω enriches the $\theta(\eta)$ when $Re_\omega = 0$. The rate of inclination of $\theta(\eta)$ significantly increases with increasing values Re_Ω . Figure 32 show the significance of Re_ω on the dimensionless $\theta(\eta)$. Raising the value of Re_ω enriches the $\theta(\eta)$ when $Re_\Omega = 1$. The rate of inclination of $\theta(\eta)$ significantly increases with increasing values Re_ω . Figure 33 depicts the nanoparticles volume segment versus the momentum distribution pattern $G(\eta)$ which enables the dissemination of the fraction of nanoparticles reduces the fluid velocity in comparison with the hybrid and trihybrid nanofluid as it increases the density of fluid. On the other way round in Figure 34 temperature raises up with the amalgamation of nanoparticles in trihybrid nanofluid. This means trihybrid nanofluid model is more appropriate. Figure 35 shows the streamlines patterns of the flow. Figure 36 represents observation of no effect of changing mesh size on the graph.

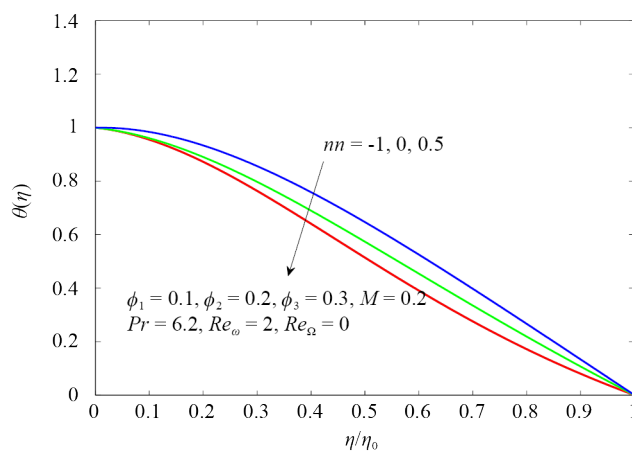


Figure 26. Between a stationary cone and a moving disc, an impression of $\theta(\eta)$ at three different radial exponents

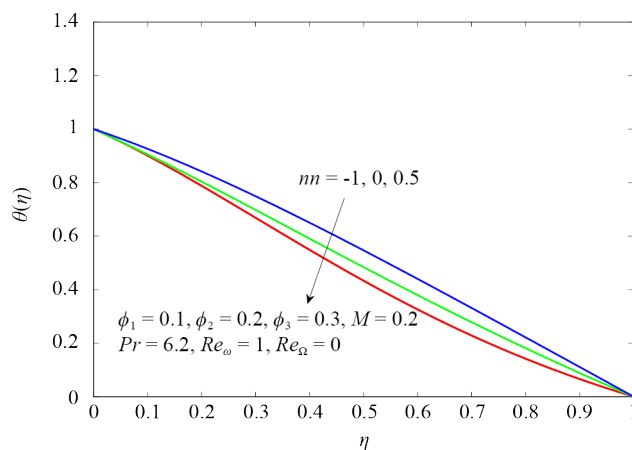


Figure 27. At three distinct radial exponents with $\frac{Re_\omega}{Re_\Omega} = 1.01$, the result of $\theta(\eta)$ between a stable disc and revolving cone

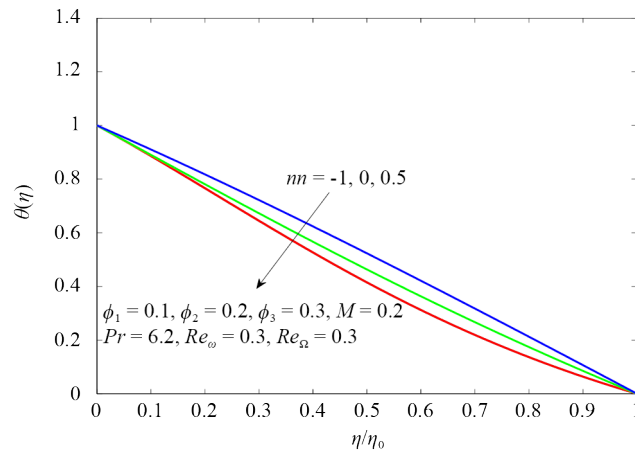


Figure 28. At three distinct radial exponents with $\frac{Re_\omega}{Re_\Omega} = 1.01$, the effect of $\theta(\eta)$ between a stagnant disc and revolving cone

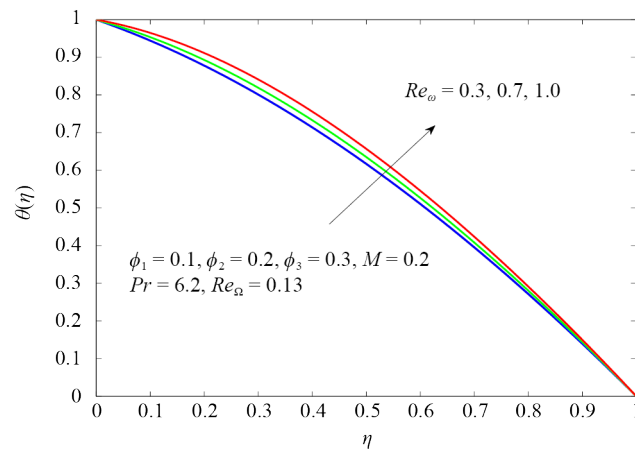


Figure 29. Image showing the interaction of a Counter-revolving disc and cone at three different radial exponents, where $Re_\omega = -Re_\Omega$. (a) $Re_\omega = 1$ (b) $Re_\Omega = 1$

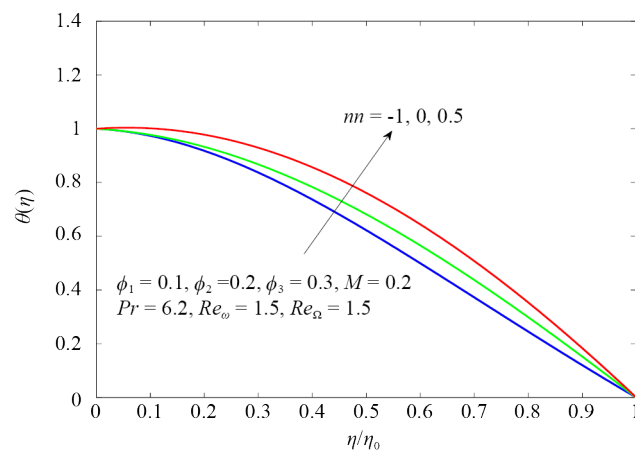


Figure 30. Image showing the interaction of inverse rotation disc and cone at three different radial exponents

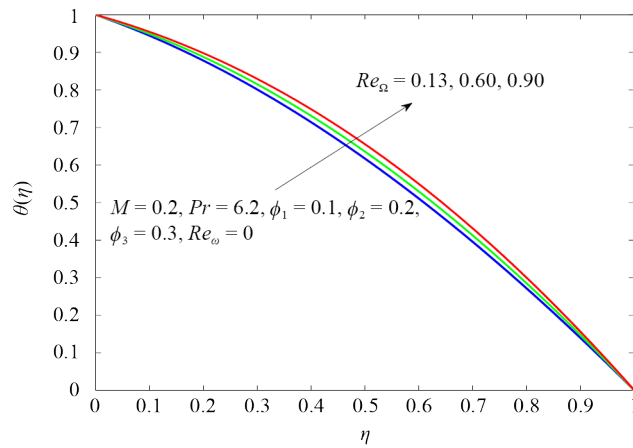


Figure 31. The outcome of Re_{Ω} against $\theta(\eta)$

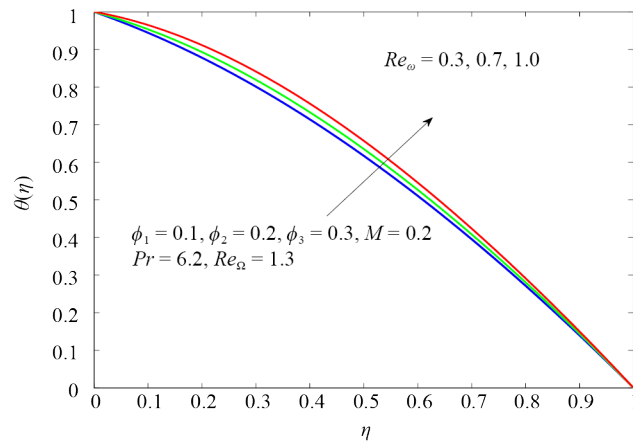


Figure 32. The implication of Re_{ω} against $\theta(\eta)$

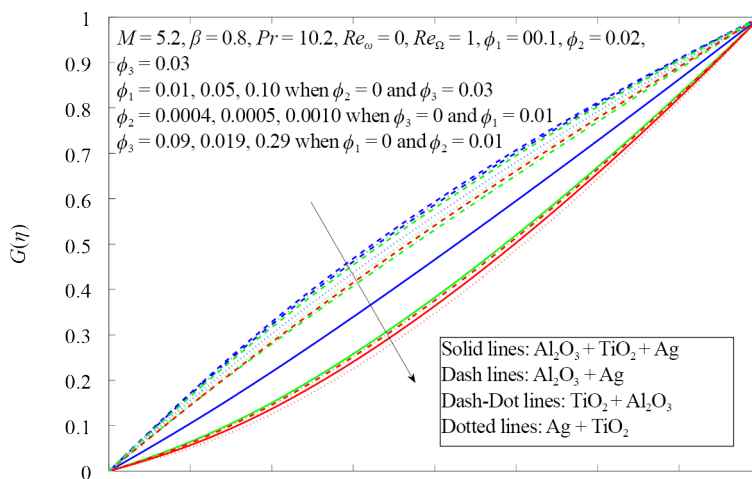


Figure 33. Velocity patterns $G(\eta)$ for hybrid and trihybrid nanofluid

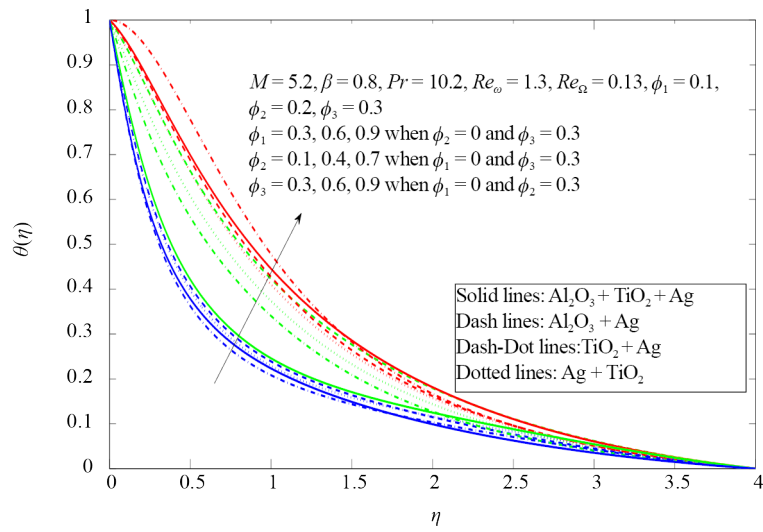


Figure 34. Temperature patterns $\theta(\eta)$ for hybrid and trihybrid nanofluid

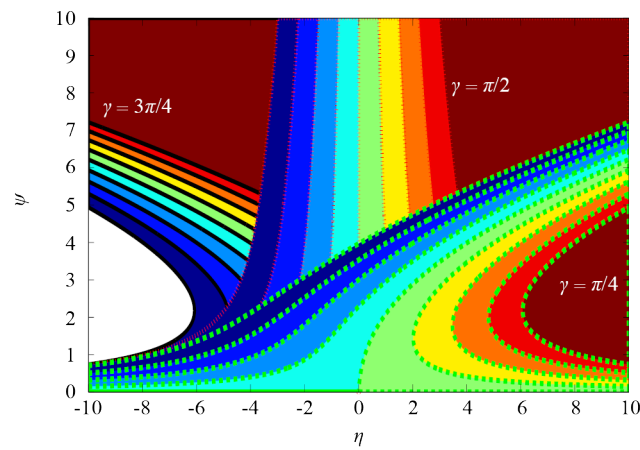


Figure 35. Streamlines

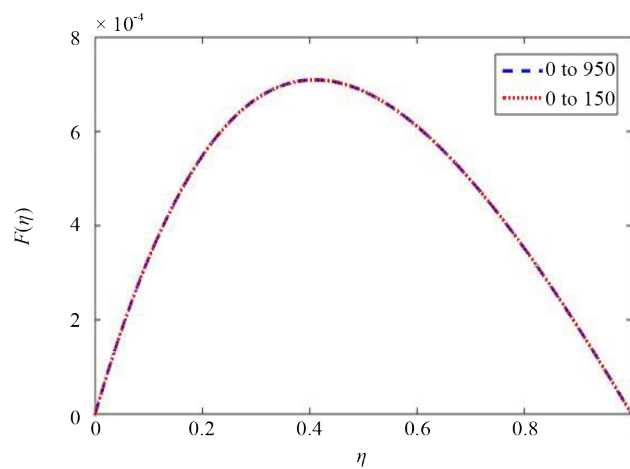


Figure 36. Grid independence patterns

Table 1 shows the rheological properties of the nanoparticles and base fluid. To strengthen the code and validity of the results, we have compared our obtained numerical results with the already published results. Table 2 shows the comparison of our obtained results in the limiting case with the results available in the literature.

Table 1. Heat-related characteristics of base fluid and tri hybrid nanoparticles

Physical properties	Blood	Al_2O_3	TiO_2	Ag [27, 40]
ρ ($kg \cdot m^{-3}$)	1,050	6,310	4,250	10.500
C_p ($J \cdot kg^{-1} \cdot K^{-1}$)	3,617	773	686.2	235
k ($W \cdot m^{-1} \cdot K^{-1}$)	0.52	32.9	8.9538	4.29
σ (S/m)	1,090	5.96×10^7	1×10^{12}	3.6×10^7

Table 2. Comparison with Wang et al. [42] in limited case

Pr	Wang et al. [42]			Current results		
	$n = -1$	$n = 0$	$n = 1$	$n = -1$	$n = 0$	$n = 1$
0.1	0.2913	0.2860	0.2752	0.2913	0.2860	0.2752
0.5	0.3021	0.2755	0.2193	0.3021	0.2755	0.2193
0.75	0.3078	0.2700	0.1883	0.3078	0.2700	0.1883
1	0.3158	0.2625	0.1436	0.3158	0.2625	0.1436

5. Concluding remarks

In the current work, genuine applications-particularly disk-cone equipment utilised in industrial settings are revisited. Considered as a particular kind of trihybrid nanoliquid made up of aluminium oxide nanoparticles (Al_2O_3), Titanium dioxide (TiO_2) and silver Ag nanoparticles along with the blood as base fluid which, whether they are believed to be fixed or moving, rotate either anticlockwise or clockwise under the influence of magnetic fields. Figures and tables illustrate the impact of physical interest variables on velocity and temperature. The following are the key findings from the study:

- A greater quantity of solid nanoparticles improves the rate of heat transfer and reduces the velocity of the carrier fluid.
- In contrast, the positive increase in the magnetic parameter M causes the flow's velocity to decrease and its temperature to rise $\theta(\eta)$.
- The $G(\eta)$ radial velocity profile is positively influenced by the local Reynold's value $Re_\omega = r^2 \omega/\nu$ and $Re_\Omega = r^2 \Omega/\nu$.
- The momentum boundary layer is expanding when the cone and disc are rotating in the same direction.
- The study results can enhance industrial processes using trihybrid Casson nanofluids by improving heat transfer, optimizing pipeline flow, and enabling smart fluid applications. This leads to more efficient and innovative processes in various industries, including biomedical applications.
- The study results can enhance industrial processes using trihybrid Casson nanofluids by improving heat transfer, optimizing pipeline flow, and enabling smart fluid applications. This leads to more efficient and innovative processes in various industries, including biomedical applications.
- Studying trihybrid Casson nanofluid computational behavior aims to predict flow and heat transfer, model non-Newtonian behavior, and validate numerical methods for reliable simulations.

■ The study aligns with previous research on enhanced thermal conductivity and non-Newtonian behavior. However, it differs in its unique trihybrid combination and investigation of Casson fluid behavior. This adds new insights to the understanding of hybrid nanofluids' complex behavior and potential applications.

This work can be extended in a variety of directions, including the exploration of different fluids with varying properties, modifications to the geometry to assess their impact on system performance, and the application of diverse boundary conditions to understand their influence on the overall behavior. Additionally, further studies could investigate the effects of scaling, introduce turbulence models, or incorporate advanced computational techniques to enhance accuracy and efficiency. By broadening the scope of the analysis, these extensions could provide deeper insights and potentially lead to optimized designs and more robust solutions for a wide range of applications.

Author's contributions

While the writeup of this article, all authors contributed equally.

Funding

This Research is funded by Researchers Supporting Project Number (RSPD2024R553), King Saud University, Riyadh, Saudi Arabia.

Conflict of interest

The authors have no competitive interests that can be influential in this paper.

References

- [1] Spruell C, Baker AB. Analysis of a high-throughput cone-and-plate apparatus for the application of defined spatiotemporal flow to cultured cells. *Biotechnology and Bioengineering*. 2013; 110(6): 1782-1793.
- [2] Fardin MA, Lerouge S. Instabilities in wormlike micelle systems: From shear-banding to elastic turbulence. *The European Physical Journal E*. 2012; 35: 1-29.
- [3] Wahid NS, Arifin NM, Khashi'ie NS, Pop I. Marangoni hybrid nanofluid flow over a permeable infinite disk embedded in a porous medium. *International Communications in Heat and Mass Transfer*. 2021; 126: 105421.
- [4] Madhukesh JK, Kumar RN, Gowda RJP, Prasannakumara BC, Ramesh GK, Khan MI, et al. Numerical simulation of AA7072-AA7075/water-based hybrid nanofluid flow over a curved stretching sheet with Newtonian heating: A non-Fourier heat flux model approach. *Journal of Molecular Liquids*. 2021; 335: 116103.
- [5] Ellahi R, Zeeshan A, Waheed A, Shehzad N, Sait SM. Natural convection nanofluid flow with heat transfer analysis of carbon nanotubes-water nanofluid inside a vertical truncated wavy cone. *Mathematical Methods in the Applied Sciences*. 2021; 46(10): 11303-11321.
- [6] Turkyilmazoglu M. On the transparent effects of Buongiorno nanofluid model on heat and mass transfer. *The European Physical Journal Plus*. 2021; 136(4): 1-15.
- [7] Nazar T, Bhatti MM, Michaelides EE. Hybrid ($Au - TiO_2$) nanofluid flow over a thin needle with magnetic field and thermal radiation: Dual solutions and stability analysis. *Microfluidics and Nanofluidics*. 2022; 26(1): 2.
- [8] Bilal M, Ramzan M, Mehmood Y, Sajid T, Shah S, Malik MY. A novel approach for EMHD Williamson nanofluid over nonlinear sheet with double stratification and Ohmic dissipation. *Proceedings of the Institution of Mechanical Engineers, Part E: Journal of Process Mechanical Engineering*. 2021. Available from: <https://doi.org/10.1177/09544089211059629>.

- [9] Zhao TH, Khan MI, Qayyum S, Kumar RN, Chu YM, Prasannakumara BC. Comparative study of ferromagnetic hybrid (manganese zinc ferrite, nickel zinc ferrite) nanofluids with velocity slip and convective conditions. *Physica Scripta*. 2021; 96(7): 075203.
- [10] Sarada K, Gowda RJP, Sarris IE, Kumar RN, Prasannakumara BC. Effect of magnetohydrodynamics on heat transfer behaviour of a non-Newtonian fluid flow over a stretching sheet under local thermal non-equilibrium condition. *Fluids*. 2021; 6(8): 264.
- [11] Khan MI, Shoaib M, Zubair G, Kumar RN, Prasannakumara BC, Mousa AAA, et al. Neural artificial networking for nonlinear Darcy-Forchheimer nanofluidic slip flow. *Applied Nanoscience*. 2023; 13(6): 3767-3786.
- [12] Kumar R, Seth GS, Bhattacharyya A. Entropy generation of von Karmans radiative flow with Al_2O_3 and Cu nanoparticles between two coaxial rotating disks: A finite-element analysis. *The European Physical Journal Plus*. 2019; 134: 1-20.
- [13] Bhattacharyya A, Seth G, Kumar R, Chamkha A. Simulation of Cattaneo-Christov heat flux on the flow of single and multi-walled carbon nanotubes between two stretchable coaxial rotating disks. *Journal of Thermal Analysis and Calorimetry*. 2020; 139: 1655-1670.
- [14] Hafeez A, Khan M, Ahmed J. Flow of Oldroyd-B fluid over a rotating disk with Cattaneo-Christov theory for heat and mass fluxes. *Computer Methods and Programs in Biomedicine*. 2020; 191: 105374.
- [15] Nazari S, Ellahi R, Sarafraz MM, Safaei MR, Asgari A, Akbari OA. Numerical study on mixed convection of a non-Newtonian nanofluid with porous media in a two lid-driven square cavity. *Journal of Thermal Analysis and Calorimetry*. 2020; 140: 1121-1145.
- [16] Ahmed J, Khan M, Ahmad L. Effectiveness of homogeneous-heterogeneous reactions in Maxwell fluid flow between two spiraling disks with improved heat conduction features. *Journal of Thermal Analysis and Calorimetry*. 2020; 139: 3185-3195.
- [17] Casson N. Flow equation for pigment-oil suspensions of the printing ink-type. *Rheology of Disperse Systems*. 1959; 1959: 84-104.
- [18] Walawender WP, Chen TY, Cala DF. An approximate Casson fluid model for tube flow of blood. *Biorheology*. 1975; 12(2): 111-119.
- [19] Batra R, Jena B. Flow of a Casson fluid in a slightly curved tube. *International Journal of Engineering Science*. 1991; 29(10): 1245-1258.
- [20] Dawar A, Shah Z, Alshehri HM, Islam S, Kumam P. Magnetized and non-magnetized Casson fluid flow with gyrotactic microorganisms over a stratified stretching cylinder. *Scientific Reports*. 2021; 11(1): 16376.
- [21] Shaheen N, Alshehri HM, Ramzan M, Shah Z, Kumam P. Soret and Dufour effects on a Casson nanofluid flow past a deformable cylinder with variable characteristics and Arrhenius activation energy. *Scientific Reports*. 2021; 11(1): 19282.
- [22] Patil A. *A Modification and Application of Parametric Continuation Method to Variety of Nonlinear Boundary Value Problems in Applied Mechanics*. New York: Rochester Institute of Technology; 2016.
- [23] Shuaib M, Shah RA, Bilal M. Variable thickness flow over a rotating disk under the influence of variable magnetic field: An application to parametric continuation method. *Advances in Mechanical Engineering*. 2020; 12(6): 1-14.
- [24] Dombovari Z, Iglesias A, Molnar TG, Habib G, Munoa J, Kuske R, et al. Experimental observations on unsafe zones in milling processes. *Philosophical Transactions of the Royal Society A*. 2019; 377(2153): 20180125. Available from: <http://doi.org/10.1098/rsta.2018.0125>.
- [25] Bilal M, Saeed A, Selim MM, Gul T, Ali I, Kumam P. Comparative numerical analysis of Maxwell's time-dependent thermo-diffusive flow through a stretching cylinder. *Case Studies in Thermal Engineering*. 2021; 27: 101301.
- [26] Smida K, Adnan, Sohail MU, Tlili I, Javed A. Numerical thermal study of ternary nanofluid influenced by thermal radiation towards convectively heated sinusoidal cylinder. *Heliyon*. 2023; 9(9): e20057.
- [27] Souayah B, Ramesh K, Hdhiri N, Yasin E, Alam MW, Alfares K, et al. Heat transfer attributes of gold-silver-blood hybrid nanomaterial flow in an EMHD peristaltic channel with activation energy. *Nanomaterials*. 2022; 12(10): 1615.
- [28] Souayah B, Ramesh K. Numerical scrutinization of ternary nanofluid flow over an exponentially stretching sheet with gyrotactic microorganisms. *Mathematics*. 2023; 11(4): 981.
- [29] Shaiq S, Shahzad A, Hayat U. A comparative investigation of magnetohydrodynamics slip $Fe_3O_4 - H_2O$ and $Al_2O_3 - H_2O$ nanofluids flow and heat transfer over an unsteady vertically curved stretching surface. *Multiscale and Multidisciplinary Modeling, Experiments and Design*. 2024; 5: 1-12.

- [30] Maraj E, Shaiq S. Rotational impact on nanoscale particles Fe_2O_4 , $NiZnFe_2O_4$, $MnZnFe_2O_4$ suspended in $C_2H_6O_2$ confined between two stretchable disks: a computational study. *Canadian Journal of Physics*. 2020; 98(3): 312-326.
- [31] Matao P, Reddy BP, Sunzu J. Hall and rotation effects on radiating and reacting MHD flow past an accelerated permeable plate with Soret and Dufour effects. *Trends in Sciences*. 2022; 19(5): 2879-2879.
- [32] Chillingo KJ, Onyango ER, Matao PM. Influence of induced magnetic field and chemically reacting on hydromagnetic Couette flow of Jeffrey fluid in an inclined channel with variable viscosity and convective cooling: A Caputo derivative approach. *International Journal of Thermofluids*. 2024; 22: 100627.
- [33] Reddy BP, Matao PM, Sunzu JM. A finite difference study of radiative mixed convection MHD heat propagating Casson fluid past an accelerating porous plate including viscous dissipation and Joule heating effects. *Heliyon*. 2024; 10(7): e28591.
- [34] Matao PM, Reddy BP, Sunzu JM. Hall and viscous dissipation effects on mixed convective MHD heat absorbing flow due to an impulsively moving vertical porous plate with ramped surface temperature and concentration. *ZAMM-Journal of Applied Mathematics and Mechanics/Zeitschrift für Angewandte Mathematik und Mechanik*. 2024; 104(5): e202300210.
- [35] Sadek O, Sadek L, Touhtouh S, Hajjaji A. The mathematical fractional modeling of TiO_2 nanopowder synthesis by sol-gel method at low temperature. *Mathematical Modeling and Computing*. 2022; 9(3): 616-626.
- [36] Pars LA. *An Introduction to the Calculus of Variations*. North Chelmsford, Massachusetts: Courier Corporation; 2013.
- [37] Sadek L. A cotangent fractional derivative with the application. *Fractal and Fractional*. 2023; 7(6): 444.
- [38] Sadek L, Lazar TA. On Hilfer cotangent fractional derivative and a particular class of fractional problems. *AIMS Mathematics*. 2023; 8(12): 28334-28352.
- [39] Farooq U, Waqas H, Fatima N, Imran M, Noreen S, Bariq A, et al. Computational framework of cobalt ferrite and silver-based hybrid nanofluid over a rotating disk and cone: a comparative study. *Scientific Reports*. 2023; 13(1): 5369.
- [40] Mumtaz M, Islam S, Ullah H, Shah Z. Chemically reactive MHD convective flow and heat transfer performance of ternary hybrid nanofluid past a curved stretching sheet. *Journal of Molecular Liquids*. 2023; 390: 123179.
- [41] Gul T, Kashifullah, Bilal M, Alghamdi W, Asjad MI, Abdeljawad T. Hybrid nanofluid flow within the conical gap between the cone and the surface of a rotating disk. *Scientific Reports*. 2021; 11(1): 1180.
- [42] Wang F, Rani P, Sarada K, Gowda RJP, Khan U, Zahran HY, et al. The effects of nanoparticle aggregation and radiation on the flow of nanofluid between the gap of a disk and cone. *Case Studies in Thermal Engineering*. 2022; 33: 101930.